Symmetry-preserving discretization of heat transfer in a complex turbulent flow

Verstappen, R.W.C.P.; Velde, R.M. van der

Published in:
Journal of Engineering Mathematics

DOI:
10.1007/s10665-006-9035-4

Publication date:
2006

Journal of Engineering Mathematics (2006) 54: 299–318
DOI 10.1007/s10665-006-9035-4

Symmetry-preserving discretization of heat transfer in a complex turbulent flow

R.W.C.P. VERSTAPPEN and R.M. VAN DER VELDE
Institute of Mathematics and Computing Science, University of Groningen, P.O.Box 800, 9700 AV Groningen, The Netherlands (E-mail: R.W.C.P.Verstappen@rug.nl)

Received 10 May 2004; accepted in revised form 26 January 2006 / Published online: 14 April 2006

Abstract. Convective and diffusive operators are discretized such that their symmetries are preserved. The resulting discretization inherits all symmetry-related properties of the continuous formulation. It is shown that a symmetry-preserving discretization is unconditionally stable and conservative. A fourth-order, symmetry-preserving discretization method is developed and tested for the numerical simulation of turbulent (flow and) heat transfer in a channel with surface-mounted cubes, where the temperature is treated as a passive scalar. The Reynolds number (based on the channel width and the mean bulk velocity) is Re=13,000. The results of the numerical simulation agree well with available experimental data.

Key words: channel flow, numerical simulation, stability, symmetry and conservation, turbulent heat transfer

1. Introduction

The smallest scales of motion in a turbulent flow result from a subtle balance between convective transport and diffusive dissipation. Therefore, in a numerical simulation method, it is important that numerical diffusion (from the convective discretization) does not interfere with physical dissipation. From a mathematical point of view, the convective and diffusive terms in the transport equations have a different structure: convection is described by a skew-symmetric differential operator (see Section 3), while diffusion is governed by a symmetric and positive semi-definite operator. With this in mind, we have developed a convective discretization method which ensures that convection is approximated by a skew-symmetric, discrete operator, whereas diffusion is discretized by a symmetric and positive semi-definite operator. The resulting discrete representation inherits all properties related to the symmetries from the continuous formulation. In particular, the (kinetic) energy of any discrete solution is conserved when the flow is inviscid, and decreases in time for viscous flow. In other words, the spatial discretization is both unconditionally stable and conservative. Second-order and fourth-order versions have been developed thus far, applicable to structured nonuniform grids [1]. The method has been termed 'symmetry-preserving discretization', as it preserves the (skew-)symmetry of the differential operators.

If the discretization scheme is constructed to minimize the local truncation error, the skew symmetry of the convective operator is lost on nonuniform grids and quantities that are conserved in the continuous formulation, like the kinetic energy, are not conserved in the discrete formulation. Manteufel and White [2] have rigorously proven that a second-order local truncation error forms a sufficient, but not a necessary, condition for the solution to be second-order. Hence, we may somewhat compromise on the local truncation error to preserve both

the symmetry of the underlying differential operator and the order of accuracy of the numerical solution.

Conservation properties have a long standing in the analysis of discretization methods for the (incompressible) Navier-Stokes equations. Morinishi *et al.* [3] have considered a family of higher-order discretization schemes for incompressible flow that almost/fully conserve mass, momentum and kinetic energy. Vasilyev [4] has generalized some of the schemes of Morinishi *et al.* [3] to nonuniform meshes while maintaining the formal, fourth-order accuracy (by means of a mapping technique), yet without sustaining the simultaneous conservation of mass, momentum and energy. Nicoud [5] considers a low-Mach-number approximation for the Navier–Stokes equations where the energy is conserved if an approximate state equation is used. Ducros *et al.* [6] deal with compressible flow. They extend Jameson's second-order finite-volume method [7] to a family of higher-order 'skew-symmetric-like' centered schemes. Finally, one could also apply the procedure for designing finite-difference schemes that inherit energy conservation from conservative p.d.e.'s by Furihata [8] and the mimetic method by Hyman *et al.* [9] for constructing finite-difference approximations of the Navier–Stokes equations that retain/mimic the main conservation properties.

The present paper deals with the extension of the symmetry-preserving discretization method to turbulent heat transfer. The effectiveness of the method is studied with the help of an analytic solution (Taylor-Green vortex with passive scalar transport), and the method is validated for turbulent flow and heat transfer in a channel. The turbulent flow and heat transfer in a channel with surface mounted cubical obstacles is then considered.

Heat transfer in a channel with surface-mounted cubical obstacles forms a generic example of a problem that occurs in many engineering applications, for instance in the design of cooling devices. It is one of the test cases in a series of Workshops on Refined Turbulence Modelling; see [10]–[12]. From these workshops, it may be concluded that the flow and heat transfer in a channel with surface-mounted cubes provides a major challenge to current Reynolds-averaged Navier–Stokes (RaNS) models. Basically, the shedding of vortices past the cubical obstacles is not described accurately by RaNS-models. An unsteady simulation in which the shedding is explicitly computed may solve this problem [13].

Both the flow and the heat transfer in a channel with surface-mounted cubes have experimentally been investigated by Meinders *et al.* [14], [15]. They have measured mean velocities and second-order moments of fluctuating velocities in the two planes that bisect the cubical obstacles. So far, the temperature has been measured at the surfaces of one heated cube only (by means of infrared thermography). Here, the flow field and temperature field are solved numerically from the unsteady Navier–Stokes equations and the energy equation, where the thermal energy equation is considered in the Boussinesq approximation, so that the temperature can be computed as a passive scalar. The Reynolds number is equal to 13,000 (based on the channel width and the mean bulk velocity); the Prandtl number equals 0·71 (air).

The paper is organized as follows. The mathematical model for the flow and the heat transfer in a channel with surface-mounted cubes is presented concisely in Section 2. In Section 3, the symmetry and conservation properties that form the basis for our numerical approach are described. The numerical method is outlined and validated in Section 4. Results for a channel with surface-mounted cubes are compared with the available experimental data in Section 5.

2. Mathematical model

This section describes a mathematical model for flow and heat transfer in a channel with surface-mounted cubes. A matrix of 25×10 cubes (each of size h^3) is mounted on one wall

of the channel. The pitch of the cubes equals $4h$, both in the streamwise and in the spanwise direction. The height of the channel is $3{\cdot}4h$. Flow measurements by Meinders [15] showed that the flow is in a fully developed, symmetrical state around the middle cube at the eighteenth row from the inlet. In other words, the influence of the inlet and outlet can be neglected there. This justifies confining the flow domain to a sub-channel unit of dimension $4h \times 3{\cdot}4h \times 4h$ with periodic boundary conditions in the streamwise and spanwise direction. Figure 1 displays a sub-channel unit.

In the flow domain, the velocity $\boldsymbol{u}$ and pressure p are described by the unsteady, incompressible Navier–Stokes equations and the continuity equation,

$$\partial_t \boldsymbol{u} + (\boldsymbol{u} \cdot \nabla)\ \boldsymbol{u} - \tfrac{1}{\mathrm{Re}}(\nabla \cdot \nabla)\boldsymbol{u} + \nabla p = \boldsymbol{0} \quad \nabla \cdot \boldsymbol{u} = 0, \tag{1}$$

with no-slip conditions at the solid walls (of both the channel and the cubes). As in the experiment, the Reynolds number is $\mathrm{Re} = 13{,}000$, based upon the channel height and bulk velocity.

In the Boussinesq approximation, the temperature, ϕ, can be computed as a passive scalar from the following convection-diffusion equation

$$\partial_t \phi + (\boldsymbol{u} \cdot \nabla)\ \phi - \tfrac{1}{\mathrm{Re\,Pr}}(\nabla \cdot \nabla)\phi = 0, \tag{2}$$

where the Prandtl number is $\mathrm{Pr} = 0{\cdot}71$. Equation (2) is the thermal-energy equation (with mechanical energy removed). Since only one cube in the array is heated in the experiment, it is not valid to assume periodicity of the temperature in the streamwise direction with the defined sub-channel unit. To model the heat transfer properly, we have doubled the computational domain in the streamwise direction. At a distance $4h$ upstream from the heated cube, the air temperature is set equal to the ambient temperature $\phi_{\mathrm{ambient}} = 290°\mathrm{K}$. At a distance $4h$ downstream (measured from the windward face of the heated cube) the normal derivative of the temperature is set to zero. This outflow condition may lead to non-physical reflections. To suppress waves being thrown back from the outflow surface, the outflow is preceded by a buffer zone (of length $0{\cdot}4h$) in which the Prandtl number Pr is decreased from $0{\cdot}71$ to $0{\cdot}2$. We have considered both Neumann and periodic conditions in the spanwise direction. They proved to be equally good. The results shown in this paper have been computed with periodic conditions in the spanwise direction. The surface temperature of the unheated cubes and that of the flat wall of the channel are set to the ambient temperature, $\phi_{\mathrm{ambient}} = 290°\mathrm{K}$. The temperature of the wall at which the heated cube is mounted is taken slightly higher, $\phi = 294°\mathrm{K}$, to model its warm-up.

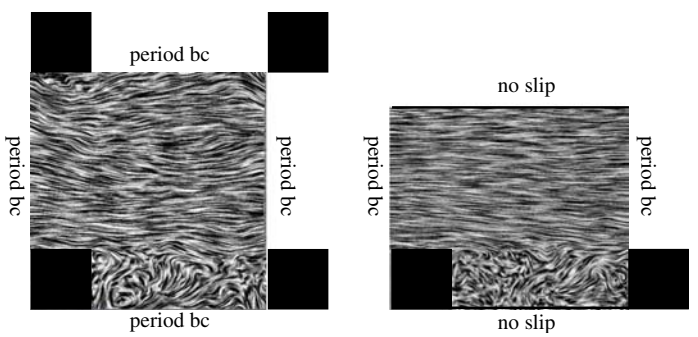

Figure 1. Top- and side-view of a sub-channel unit. Both pictures show the instantaneous flow field (taken from the DNS) in the plane that bisects the cubes.

The heated cube is made of a copper core covered by an epoxy layer of thickness $h/10$. The copper core is kept at a constant temperature of $\phi = 348°\mathrm{K}$. In the epoxy layer, the temperature is governed by an unsteady diffusion equation

$$\partial_t \phi - \mathrm{D}_{\mathrm{epoxy}}(\nabla \cdot \nabla)\phi = 0, \tag{3}$$

where the thermal diffusivity $\mathrm{D}_{\mathrm{epoxy}}$ of epoxy $\mathrm{D}_{\mathrm{epoxy}} = 1{\cdot}206 \times 10^{-7}\,\mathrm{W/m^2\,K}$ [15].

At the five faces of the heated cube that are cooled by the air flow, the air temperature equals that of epoxy, and the flux satisfies

$$\underset{\text{(conduction)}}{-\lambda\,\frac{\partial\phi}{\partial n}|_{\mathrm{epoxy}}} \;=\; \underset{\text{(convection)}}{-\lambda\,\frac{\partial\phi}{\partial n}|_{\mathrm{air}}} \;+\; \underset{\text{(radiation)}}{\epsilon\sigma\,\left(\phi^4_{\mathrm{face}} - \phi^4_{\mathrm{ambient}}\right)}, \tag{4}$$

where ϕ_{face} stands for the average temperature at a face of the cube, and n denotes the outward unit normal (as seen from the cube). The conductivity of epoxy λ_{epoxy}, the surface emissivity ϵ, and the Stefan–Boltzmann constant σ are set equal to their experimentally determined values. According to Meinders [15] they are $0{\cdot}237\,\mathrm{W/mK}$, $0{\cdot}95$ and $5{\cdot}670 \times 10^{-8}\,\mathrm{W/m^2\,K^4}$, respectively. The conductivity of air is taken as $\lambda_{\mathrm{air}} = 0{\cdot}024\,\mathrm{W/mK}$. Note that the radiation is modeled in terms of the average temperature on a face. Hence, the radiation is constant per face.

The boundary conditions are summarized in Figure 2.

The geometry of the interface between the heated cubical obstacle and the channel wall is rather complex in the experimental setting. It consists of screws, wires, etc. We have disregarded all these elements. Instead, we have simply continued the epoxy layer near the interface. In addition, we have assumed that the temperature at the under-surface of the channel wall (which is approximately 8 mm thick in the experiment) equals the ambient temperature. Then we may obtain a boundary condition by performing a linear interpolation between the epoxy temperature in the cube nearest to the upper-surface of the channel wall and the ambient temperature at the under-surface of the channel wall right under the cube.

3. Symmetry and conservation properties

The skew symmetry of the convective operator $(\boldsymbol{u} \cdot \nabla)\boldsymbol{v}$

$$((\boldsymbol{u} \cdot \nabla)\boldsymbol{v}, \boldsymbol{w}) = -(\boldsymbol{v}, (\boldsymbol{u} \cdot \nabla)\boldsymbol{w}) \tag{5}$$

implies that the solution of Equation (1), as well as the solution of Equation (2), have fundamental conservation properties (in the absence of diffusion, of course). To illustrate one of these properties, we introduce the kinetic energy. In terms of the usual scalar product $(\boldsymbol{u}, \boldsymbol{v}) = \int_\Omega \boldsymbol{u} \cdot \boldsymbol{v}\,\mathrm{d}x$,

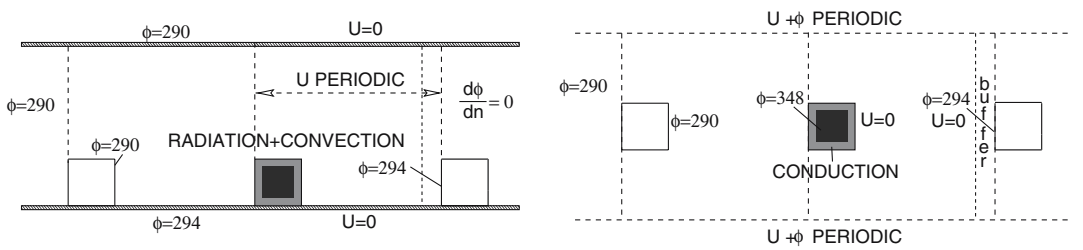

Figure 2. Overview of the boundary conditions. The picture on the left shows a side-view of the channel; the one on the right displays a top-view.

the kinetic energy of a fluid with velocity $\boldsymbol{u}$ occupying a region Ω is given by $|\boldsymbol{u}|^2 = (\boldsymbol{u}, \boldsymbol{u})$. The norm of ϕ is defined as $|\phi|^2 = \int_\Omega \phi^2 \, \mathrm{d}x$.

The evolution of the kinetic energy follows from differentiating $(\boldsymbol{u}, \boldsymbol{u})$ with respect to time and rewriting $\partial_t \boldsymbol{u}$ with the help of (1). In this way, we get a convective contribution given by $((\boldsymbol{u} \cdot \nabla)\boldsymbol{u}, \boldsymbol{u}) + (\boldsymbol{u}, (\boldsymbol{u} \cdot \nabla))$. This term cancels as a result of Equation (5). The pressure does not contribute either, since $\nabla \cdot \boldsymbol{u} = 0$. Thus, after some algebra, we get (ignoring boundary terms)

$$\frac{\mathrm{d}}{\mathrm{d}t}|\boldsymbol{u}|^2 = -\tfrac{2}{\mathrm{Re}}|\nabla \boldsymbol{u}|^2 \leq 0. \tag{6}$$

The same reasoning applies to the evolution of the L2 norm of ϕ,

$$\frac{\mathrm{d}}{\mathrm{d}t}|\phi|^2 = -\tfrac{2}{\mathrm{Re}\,\mathrm{Pr}}|\nabla \phi|^2 \leq 0, \tag{7}$$

where the convective contribution $((\boldsymbol{u} \cdot \nabla)\phi, \phi) + (\phi, (\boldsymbol{u} \cdot \nabla)\phi)$ cancels once again as a consequence of the skew symmetry given by (5).

To prove Equation (5) we use the identity

$$\nabla \cdot (f \boldsymbol{u}) = f \nabla \cdot \boldsymbol{u} + \nabla f \cdot \boldsymbol{u},$$

which holds for any (differentiable) scalar field f and vector field $\boldsymbol{u}$. Taking $f = \boldsymbol{v} \cdot \boldsymbol{w}$, $\nabla \cdot \boldsymbol{u} = 0$ and applying Gauß's Divergence Theorem gives

$$\begin{aligned}\int_{\partial\Omega} (\boldsymbol{v} \cdot \boldsymbol{w})(\boldsymbol{u} \cdot \boldsymbol{n}) \mathrm{d}s &= \int_\Omega \nabla \cdot ((\boldsymbol{v} \cdot \boldsymbol{w})\boldsymbol{u}) \, \mathrm{d}\Omega = \int_\Omega \nabla(\boldsymbol{v} \cdot \boldsymbol{w}) \cdot \boldsymbol{u} \mathrm{d}\Omega \\ &= \int_\Omega (\boldsymbol{u} \cdot \nabla)\boldsymbol{v} \cdot \boldsymbol{w} \mathrm{d}\Omega + \int_\Omega (\boldsymbol{u} \cdot \nabla)\boldsymbol{w} \cdot \boldsymbol{v} \mathrm{d}\Omega,\end{aligned}$$

which shows that the trilinear form $((\boldsymbol{u} \cdot \nabla)\boldsymbol{v}, \boldsymbol{w})$ is skew-symmetric with respect to $\boldsymbol{v}$ and $\boldsymbol{w}$ provided the boundary term vanishes. The latter condition is satisfied if either the normal velocity $\boldsymbol{u} \cdot \boldsymbol{n}$ vanishes at the boundary $\partial\Omega$ of the flow domain Ω, or $\boldsymbol{v} \cdot \boldsymbol{w}$ vanishes, or periodic boundary conditions apply.

Finally, it may be remarked that the skew symmetry (5) is one of the key elements of the mathematical theory of the Navier–Stokes equations, as discussed in the monograph [16].

4. Numerical method

We construct fourth-order, finite-volume discretizations of convective and diffusive differential operators in (1) and (2) that preserve the respective symmetries on nonuniform grids. That is, we want to discretize the convective operator $(\boldsymbol{u} \cdot \nabla)\boldsymbol{v}$ such that (5) is preserved and the discrete diffusive operator is symmetric and positive semi-definite so that the inequalities (6) and (7) hold discretely too. This section describes: the symmetry-preserving spatial discretization (Section 4.1), the temporal integration (Section 4.2), and the validation of the numerical method (Section 4.3).

4.1. Symmetry-preserving spatial discretization

The basic idea of the symmetry-preserving discretization method is outlined (with the help of a linear convection-diffusion equation in one spatial dimension) in Section 4.1.1. In Section 4.1.2, the application of the method to the incompressible Navier–Stokes equation is sketched briefly. For a more detailed discussion the reader is referred to [1]. The method is extended to the scalar transport equation (2) in Section 4.1.3.

4.1.1. *Basic idea*

To illustrate the basic idea in one spatial dimension, we consider the interval (a, b) and impose periodic boundary conditions. The inner product of two functions $u(x)$ and $v(x)$ is given by $(u, v) = \int_a^b u(x)v(x)\mathrm{d}x$, and the convective derivative reads $\bar{u}\partial_x u$, where the convective transport velocity $\bar{u}$ is taken constant, for simplicity. Integration by parts yields the skew symmetry

$$(\bar{u}\partial_x u, v) = -(u, \bar{u}\partial_x v)\,. \tag{8}$$

In the same manner it can be shown that $-\partial_{xx}^2$ is symmetric, positive and semi-definite. The kinetic energy $|u|^2$ of any solution of the convection-diffusion equation

$$\partial_t u + \bar{u}\partial_x u - \tfrac{1}{\mathrm{Re}}\partial_{xx}^2 u = 0 \tag{9}$$

is governed by

$$\frac{\mathrm{d}}{\mathrm{d}t}|u|^2 = -(\bar{u}\partial_x u, u) - (u, \bar{u}\partial_x u) + \tfrac{1}{\mathrm{Re}}(u, \partial_{xx}^2 u) + \tfrac{1}{\mathrm{Re}}(\partial_{xx}^2 u, u) = -\tfrac{2}{\mathrm{Re}}(\partial_x u, \partial_x u) \;\leq\; 0, \tag{10}$$

where the convective contribution cancels because of (8); compare (10) with (6).

Derivatives are often discretized so that the order of the local truncation error becomes as large as possible. For a stencil consisting of three points, x_{i-1}, x_i, and x_{i+1}, this approach leads to the approximation

$$\partial_x u\,(x_i) \approx \frac{\delta x_i^2 u_{i+1} + (\delta x_{i+1}^2 - \delta x_i^2)u_i - \delta x_{i+1}^2 u_{i-1}}{\delta x_{i+1}\delta x_i(\delta x_{i+1} + \delta x_i)}, \tag{11}$$

where the grid spacing is denoted by $\delta x_i = x_i - x_{i-1}$. Approximation (11) may also be derived by constructing a parabola through the three given data points $\left(x_{i-1}, u_{i-1}\right)$, (x_i, u_i) and $\left(x_{i+1}, u_{i+1}\right)$ and differentiating that parabola at the central point x_i of the stencil.

The Lagrangian discretization (11) is applied to Equation (9) in order to analyze its conservation and stability properties. In matrix-vector notation, the dynamics of the spatially discrete velocity vector $\boldsymbol{u}_h$ is governed by the following finite-volume discretization of the convection-diffusion equation (9)

$$\boldsymbol{\Omega}_0\frac{\mathrm{d}\boldsymbol{u}_h}{\mathrm{d}t} + \boldsymbol{C}_0(\bar{u})\boldsymbol{u}_h + \boldsymbol{D}_0\boldsymbol{u}_h = \boldsymbol{0}, \tag{12}$$

where the discrete velocities u_i constitute the vector $\boldsymbol{u}_h$, and the diagonal matrix $\boldsymbol{\Omega}_0$ is built of the finite volumes: $(\boldsymbol{\Omega}_0)_{i,i} = \frac{1}{2}(x_{i+1} - x_{i-1})$. The tridiagonal matrices $\boldsymbol{C}_0(\bar{u})$ and $\boldsymbol{D}_0$ represent the discrete convective and diffusive fluxes, respectively.

In the absence of diffusion, that is for $\boldsymbol{D}_0 = \boldsymbol{0}$, the kinetic energy $||\boldsymbol{u}_h||^2 = \boldsymbol{u}_h^*\boldsymbol{\Omega}_0\boldsymbol{u}_h$ of any solution $\boldsymbol{u}_h$ of the dynamical system (12) is conserved if and only if the right-hand side of

$$\frac{\mathrm{d}}{\mathrm{d}t}||\boldsymbol{u}_h||^2 = -\boldsymbol{u}_h^*\left(\boldsymbol{C}_0(\bar{u}) + \boldsymbol{C}_0^*(\bar{u})\right)\boldsymbol{u}_h$$

is zero. This conservation property holds (for any real $\boldsymbol{u}_h$) if and only if the coefficient matrix $\boldsymbol{C}_0(\bar{u})$ is skew-symmetric,

$$\boldsymbol{C}_0(\bar{u}) + \boldsymbol{C}_0^*(\bar{u}) = \boldsymbol{0}. \tag{13}$$

Note that we can make use of the theorem $\boldsymbol{x}^*\boldsymbol{A}\boldsymbol{x} = 0$ for all real vectors $\boldsymbol{x}$ if and only if the square matrix $\boldsymbol{A}$ is skew-symmetric; see for instance [17, p. 68]. In conclusion, the discrete

operator $\boldsymbol{C}_0(\bar{u})$ has to inherit the skew symmetry of the continuous convective derivative $\bar{u}\partial_x$: compare Equation (13) with (8).

We see immediately that the discretization given by (11) leads to a coefficient matrix $\boldsymbol{C}_0(\bar{u})$ with nonzero diagonal entries (for nonuniform grids). Hence, the approach described by (11) violates the skew-symmetry condition (13). Thus, if the discretization scheme is constructed to minimize the local truncation error, the skew symmetry of the convective operator is lost on nonuniform grids, and quantities that are conserved in the continuous formulation, like the kinetic energy, are not conserved in the discrete formulation.

Here, it may be noted that we have defined the discrete kinetic energy in conformity with the rule applied to derive the finite-volume discretization (12). That is, the integral of $\partial_t \boldsymbol{u}$ over the control volume $\frac{1}{2}(x_{i+1}-x_{i-1})$ is discretized by $\mathrm{d}_t\,(\Omega_0 \boldsymbol{u}_h)_i$, and the energy integrated over this control volume is approximated by the product of $(\boldsymbol{u}_h)_i$ and $(\Omega_0 \boldsymbol{u}_h)_i$. This is the obvious definition of the discrete kinetic energy. Yet, one may consider other definitions. In general, if one defines the discrete kinetic by $||\boldsymbol{u}_h||_A^2 = \boldsymbol{u}_h^* \boldsymbol{A} \boldsymbol{u}_h$, with $\boldsymbol{A}$ a positive-definite matrix, one gets (for $\boldsymbol{D}_0 = \boldsymbol{0}$)

$$\frac{\mathrm{d}}{\mathrm{d}t}||\boldsymbol{u}_h||_A^2 = -\boldsymbol{u}_h^* \left(\boldsymbol{A}\boldsymbol{\Omega}_0^{-1}\boldsymbol{C}_0(\bar{u}) + (\boldsymbol{A}\boldsymbol{\Omega}_0^{-1}\boldsymbol{C}_0)^*(\bar{u}) \right) \boldsymbol{u}_h.$$

Hence, the energy $||\boldsymbol{u}_h||_A^2$ is conserved (in the absence of diffusion) if and only if $\boldsymbol{B}\boldsymbol{C}_0(\bar{u})$ is skew-symmetric,

$$\boldsymbol{B}\boldsymbol{C}_0(\bar{u}) + \boldsymbol{C}_0^*(\bar{u})\boldsymbol{B}^* = \boldsymbol{0}, \tag{14}$$

where $\boldsymbol{B} = \boldsymbol{A}\boldsymbol{\Omega}_0^{-1}$. Now, suppose that (i) $\boldsymbol{C}_0$ is similar to a diagonal matrix $\boldsymbol{\Lambda}$ with purely imaginary entries, that is $\boldsymbol{C}_0 = \boldsymbol{P}^{-1}\boldsymbol{\Lambda}\boldsymbol{P}$, and (ii) $\boldsymbol{C}_0$ is not skew-symmetric, *i.e.*, Equation (13) is not satisfied. Then, Equation (14) may be solved by taking $\boldsymbol{B} = \boldsymbol{P}^*\boldsymbol{P}$. In other words, Equation (13) restricts the discretization of the convective fluxes to skew-symmetric matrices, which have purely imaginary eigenvalues, whereas Equation (14) allows other (non-skew-symmetric) matrices that have purely imaginary eigenvalues. Note that framing the discussion in terms of purely imaginary eigenvalues still rules out (11): a straightforward computation shows that the trace of $\boldsymbol{C}_0$ is nonzero if (11) is applied on a nonuniform grid. Consequently, $\boldsymbol{C}_0$ does not have purely imaginary eigenvalues if the convective derivative is discretized according to (11). In the remainder, we will take $\boldsymbol{A} = \boldsymbol{\Omega}$; hence $\boldsymbol{B} = \boldsymbol{I}$, meaning that we adopt the obvious definition of the discrete kinetic energy. Therefore, we will construct coefficient matrices $\boldsymbol{C}_0$ that satisfy (13). The generalized symmetry condition (14) does not fall within the scope of the present paper.

As remarked before, the discretization (11) that minimizes the local truncation error does not satisfy (13) on nonuniform grids. Therefore, rather than concentrating on reducing the local truncation error, we select the discretization on the basis of symmetry and thus write

$$\bar{u}\,\partial_x u(x_i) \approx \bar{u}\,\frac{u_{i+1}-u_{i-1}}{x_{i+1}-x_{i-1}} = \left(\boldsymbol{\Omega}_0^{-1}\boldsymbol{C}_0(\bar{u})\boldsymbol{u}_h \right)_i. \tag{15}$$

The entries of the tridiagonal matrix $\boldsymbol{C}_0(\bar{u})$ are now given by $\boldsymbol{C}_0(\bar{u})_{i,i-1} = -\frac{1}{2}\bar{u}$, $\boldsymbol{C}_0(\bar{u})_{i,i} = 0$ and $\boldsymbol{C}_0(\bar{u})_{i,i+1} = \frac{1}{2}\bar{u}$. Hence, $\boldsymbol{C}_0(\bar{u})$ satisfies (13).

The symmetry-preserving discretization (15) may not seem accurate at first sight, as the derivative is simply approximated by drawing a straight line from (x_{i-1}, u_{i-1}) to (x_{i+1}, u_{i+1}). The local truncation error is indeed only first-order, unless the grid is almost uniform. Yet, the order of the local truncation error is not decisive. Given stability, a second-order local truncation error is a sufficient, but not necessary, condition for the solution to be of second

order. Manteufel and White [2] have rigorously proved that the approximation (15) yields second-order accurate solutions on uniform as well as on nonuniform meshes. The basis of their reasoning is that the approximation (15) may also be derived by the coordinate transformation $x = x(\xi)$, which maps the nonuniform grid in x onto a uniform grid in ξ. Prior to discretization, the (partial) derivative of u with respect to x is rewritten as a quotient of derivatives with respect to ξ

$$\frac{\partial u}{\partial x} = \frac{\partial u}{\partial \xi}\frac{\mathrm{d}\xi}{\mathrm{d}x} = \frac{\partial u}{\partial \xi} \Big/ \frac{\mathrm{d}x}{\mathrm{d}\xi}.$$

The two ξ-derivatives on the right-hand side are discretized on the ξ-grid, which has a uniform spacing h,

$$\frac{\partial u}{\partial \xi}(\xi_i) = \frac{u_{i+1} - u_{i-1}}{2h} + O(h^2),$$

and

$$\frac{\mathrm{d}x}{\mathrm{d}\xi}(\xi_i) = \frac{x_{i+1} - x_{i-1}}{2h} + O(h^2).$$

Neglecting the $O(h^2)$-terms in the above expressions results in the approximation (15). This alternative derivation illustrates the second-order accuracy of the skew-symmetric discretization (15) on nonuniform grids.

Diffusion is discretized in the same vein. The resulting coefficient matrix $\boldsymbol{D}_0$ is positive semi-definite, like the underlying differential operator $-\partial_{xx}^2$. Consequently, the kinetic energy of any solution of (12)–(13) cannot increase in time,

$$\frac{\mathrm{d}}{\mathrm{d}t}||\boldsymbol{u}_h||^2 = -\boldsymbol{u}_h^* \left(\boldsymbol{D}_0 + \boldsymbol{D}_0^*\right) \boldsymbol{u}_h \leq 0$$

Hence, the semi-discrete system (12) is stable on any grid if $\boldsymbol{C}_0$ is skew-symmetric and if $\boldsymbol{D}_0 + \boldsymbol{D}_0^*$ positive semi-definite. Finally, it may be noted that the inequality above underlies the discretization of (10).

4.1.2. *Symmetry-preserving discretization of the Navier–Stokes equations*

The temporal evolution of the discrete velocity vector $\boldsymbol{u}_h$ is governed by a finite-volume discretization of the incompressible Navier–Stokes equations,

$$\boldsymbol{\Omega}_\mathrm{u}\frac{\mathrm{d}\boldsymbol{u}_h}{\mathrm{d}t} + \boldsymbol{C}_\mathrm{u}(\boldsymbol{u}_h)\,\boldsymbol{u}_h + \boldsymbol{D}_\mathrm{u}\boldsymbol{u}_h - \boldsymbol{M}_\mathrm{u}^*\boldsymbol{p}_h = \boldsymbol{0}, \qquad \boldsymbol{M}_\mathrm{u}\boldsymbol{u}_h = \boldsymbol{0}, \tag{16}$$

where the vector $\boldsymbol{p}_h$ denotes the discrete pressure, $\boldsymbol{\Omega}_\mathrm{u}$ is a (positive-definite) diagonal matrix representing the sizes of the control volumes for the discrete velocities, $\boldsymbol{C}_\mathrm{u}(\boldsymbol{u}_h)$ is built from the convective flux contributions through the control faces, $\boldsymbol{D}_\mathrm{u}$ contains the diffusive fluxes, and $\boldsymbol{M}_\mathrm{u}$ is the coefficient matrix of the discretization of the integral form of the conservation of mass law; the gradient matrix, describing the integration of the pressure gradient over the control volumes $\boldsymbol{\Omega}_\mathrm{u}$, is given by $-\boldsymbol{M}_\mathrm{u}^*$. For a precise definition of the matrices $\boldsymbol{C}_\mathrm{u}(\boldsymbol{u}_h)$, $\boldsymbol{D}_\mathrm{u}$ and $\boldsymbol{M}_\mathrm{u}$, we refer to [1]. The essence of symmetry-preserving discretization is that the coefficient matrix $\boldsymbol{C}_\mathrm{u}(\boldsymbol{u}_h)$ is skew-symmetric, *i.e.*,

$$\boldsymbol{C}_\mathrm{u}(\boldsymbol{u}_h) + \boldsymbol{C}_\mathrm{u}^*(\boldsymbol{u}_h) = \boldsymbol{0}, \tag{17}$$

whereas $\boldsymbol{D}_\mathrm{u}$ is positive semi-definite. Under these two conditions, the evolution of the discrete kinetic energy $\boldsymbol{u}_h^* \boldsymbol{\Omega}_\mathrm{u} \boldsymbol{u}_h$ of any solution $\boldsymbol{u}_h$ of (16) is governed by

$$\frac{\mathrm{d}}{\mathrm{d}t}||\boldsymbol{u}_h||^2 = \frac{\mathrm{d}}{\mathrm{d}t}(\boldsymbol{u}_h^* \boldsymbol{\Omega}_\mathrm{u} \boldsymbol{u}_h) \overset{(16)}{=} -\boldsymbol{u}_h^* (\boldsymbol{C}_\mathrm{u} + \boldsymbol{C}_\mathrm{u}^*) \boldsymbol{u}_h - \boldsymbol{u}_h^* (\boldsymbol{D}_\mathrm{u} + \boldsymbol{D}_\mathrm{u}^*) \boldsymbol{u}_h \overset{(17)}{=} -\boldsymbol{u}_h^* (\boldsymbol{D}_\mathrm{u} + \boldsymbol{D}_\mathrm{u}^*) \boldsymbol{u}_h \leq 0, \tag{18}$$

where the right-hand side is zero if and only if the discrete velocity $\boldsymbol{u}_h$ lies in the null space of $\boldsymbol{D}_\mathrm{u} + \boldsymbol{D}_\mathrm{u}^*$.

Equation (17) forms the discrete representation of Equation (5): if the scalar product $(\boldsymbol{u}, \boldsymbol{v}) = \int_\Omega \boldsymbol{u} \cdot \boldsymbol{v} \mathrm{d}\boldsymbol{x}$ of two continuous functions $\boldsymbol{u}$ and $\boldsymbol{v}$ is approximated by $\boldsymbol{u}_h^* \boldsymbol{\Omega}_\mathrm{u} \boldsymbol{v}_h$, we have

$$((\boldsymbol{u} \cdot \nabla)\boldsymbol{v}, \boldsymbol{w}) \approx (\boldsymbol{C}_\mathrm{u}(\boldsymbol{u}_h)\, \boldsymbol{v}_h)^* \boldsymbol{w}_h \overset{(17)}{=} -\boldsymbol{v}_h^* \boldsymbol{C}_\mathbf{u}(\boldsymbol{u}_h)\, \boldsymbol{w}_h \approx -(\boldsymbol{v}, (\boldsymbol{u} \cdot \nabla)\boldsymbol{w}),$$

for all discrete velocity-vectors $\boldsymbol{u}_h$, $\boldsymbol{v}_h$ and $\boldsymbol{w}_h$. Equation (18) forms the discrete representation of Equation (6): the discrete (kinetic) energy is conserved if diffusion is turned off; with diffusion included, that is for $\boldsymbol{D}_\mathrm{u} \neq \boldsymbol{0}$, the right-hand side of (18) is negative for all $\boldsymbol{u}_h$ (outside the null space of $\boldsymbol{D}_\mathrm{u}$), since $\boldsymbol{D}_\mathrm{u} + \boldsymbol{D}_\mathrm{u}^*$ is positive semi-definite. In conclusion, the kinetic energy $||\boldsymbol{u}_h||^2$ of the discrete system (1) does not increase in time if the discrete, convective operator $\boldsymbol{C}_u(\boldsymbol{u}_u)$ is skew-symmetric and $\boldsymbol{D}_\mathrm{u} + \boldsymbol{D}_\mathrm{u}^*$ is positive semi-definite. The semi-discrete system (16) is stable under these conditions: a solution of (16) can be obtained on any grid, and there is no need to add an artificial damping mechanism to stabilize the spatial discretization.

Finally, it may be noted that the total momentum $\boldsymbol{u}_h^* \boldsymbol{\Omega}_\mathrm{u} \boldsymbol{1}$ (where the constant vector has as many entries as there are control volumes for the discrete velocities) is conserved,

$$\frac{\mathrm{d}}{\mathrm{d}t}\left(\boldsymbol{1}^* \boldsymbol{\Omega}_\mathrm{u} \boldsymbol{u}_h\right) = -\boldsymbol{1}^* \left(\boldsymbol{C}_\mathrm{u}(\boldsymbol{u}_h) + \boldsymbol{D}_\mathrm{u}\right) \boldsymbol{u}_h + \boldsymbol{1}^* \boldsymbol{M}_\mathrm{u}^* \boldsymbol{p}_h = \boldsymbol{C}_\mathrm{u}(\boldsymbol{u}_h) \boldsymbol{1}^* \boldsymbol{u}_h - \boldsymbol{D}_\mathrm{u} \boldsymbol{1}^* \boldsymbol{u}_h + \boldsymbol{M}_\mathrm{u} \boldsymbol{1}^* \boldsymbol{p}_h = 0,$$

since $\boldsymbol{C}_\mathrm{u}(\boldsymbol{u}_h)$ is skew-symmetric, $\boldsymbol{D}_\mathrm{u}$ is symmetric, and the constant vector lies in the null space of $\boldsymbol{C}_\mathrm{u}(\boldsymbol{u}_h)$, $\boldsymbol{D}_\mathrm{u}$ and $\boldsymbol{M}_\mathrm{u}$.

4.1.3. *Symmetry-preserving discretization of the scalar transport equation (2)*

In this section, the scalar transport equation (2) is considered in two spatial dimensions; the extension to 3D is straightforward. Figure 3 defines the discrete velocities $(u_{i,j}, v_{i,j})$ and temperature $\phi_{i,j}$.

For an incompressible fluid, the mass of any control volume $\Omega_{i,j} = [x_{i-1}, x_i] \times [y_{j-1}, y_j]$ is conserved,

$$\bar{u}_{i,j} + \bar{v}_{i,j} - \bar{u}_{i-1,j} - \bar{v}_{i,j-1} = 0, \tag{19}$$

where $\bar{u}_{i,j}$ denotes the mass flux through the face $y = y_j$ of the grid cell $\Omega_{i,j}$, and $\bar{v}_{i,j}$ stands for the mass flux through the grid face $x = x_i$,

$$\bar{u}_{i,j} = \int_{y_{j-1}}^{y_j} u(x_i, y, t)\mathrm{d}y \quad \text{and} \quad \bar{v}_{i,j} = \int_{x_{i-1}}^{x_i} v(x, y_j, t)\mathrm{d}x. \tag{20}$$

The mass fluxes in (20) are discretized by means of the mid-point rule. In matrix-vector form, the conservation-of-mass law (19) may then be written as $\boldsymbol{M}_1^\mathrm{u} \boldsymbol{u}_h = \boldsymbol{0}$.

As the mass and the scalar ϕ are transported at equal velocities, the mass flux is used to discretize the convection of the scalar ϕ through the boundaries of the grid cell $\Omega_{i,j}$,

$$|\Omega_{i,j}| \frac{\mathrm{d}\phi_{i,j}}{\mathrm{d}t} + \bar{u}_{i,j} \phi_{i+1/2,j} + \bar{v}_{i,j} \phi_{i,j+1/2} - \bar{u}_{i-1,j} \phi_{i-1/2,j} - \bar{v}_{i,j-1} \phi_{i,j-1/2}. \tag{21}$$

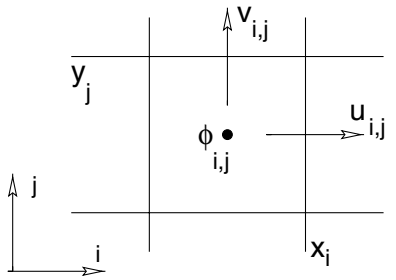

Figure 3. Location of the discrete velocity and temperature. The velocity perpendicular to a grid face is defined at the mid of that face, as in [18]. The discrete temperature is defined in the centre of a grid cell.

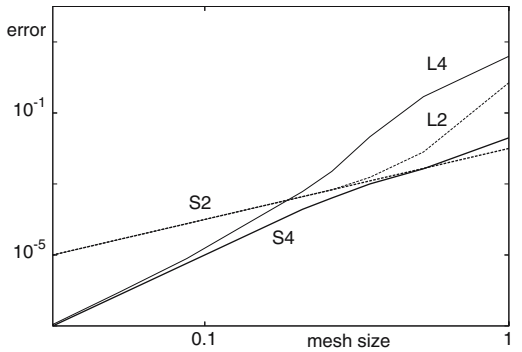

Figure 4. Global error as function of the mean mesh size on a piecewise uniform grid. Four methods are shown: 2l and 4L (second- and fourth-order Lagrangian), 2S and 4S (second- and fourth-order symmetry-preserving).

The non-integer indices refer to temperatures at the faces of the control volume $\Omega_{i,j}$ for the temperature $\phi_{i,j}$. For example, $\phi_{i-1/2,j}$ stands for the discrete temperature at the interface of $\Omega_{i-1,j}$ and $\Omega_{i,j}$. The temperature at these control faces is approximated by

$$\phi_{i+1/2,j} = \tfrac{1}{2}(\phi_{i+1,j} + \phi_{i,j}) \quad \text{and} \quad \phi_{i,j+1/2} = \tfrac{1}{2}(\phi_{i,j+1} + \phi_{i,j}). \tag{22}$$

On nonuniform grids, one would be tempted to tune the weights $\frac{1}{2}$ in the interpolation (22) to the local mesh size in order to optimize the (formal) order of the local truncation error. In doing so, the skew symmetry of the underlying convective differential operator is lost. Therefore, we take constant weights $\frac{1}{2}$, also on non-uniform meshes. To illustrate this, we regard Equations (21)–(22) as expressions for the discrete temperatures, where the mass fluxes $\bar{u}$ and $\bar{v}$ form the coefficients. Thus, we can write the (semi-)discretization in matrix-vector notation as

$$\boldsymbol{\Omega}_1 \frac{\mathrm{d}\boldsymbol{\phi}_h}{\mathrm{d}t} + \boldsymbol{C}_1(\bar{\boldsymbol{u}})\boldsymbol{\phi}_h, \tag{23}$$

where $\boldsymbol{\phi}_h$ denotes the vector with elements $\phi_{i,j}$; $\boldsymbol{\Omega}_1$ is a (positive-definite) diagonal matrix representing the sizes of the control volumes $|\Omega_{i,j}|$, whereas $\boldsymbol{C}_1(\bar{\boldsymbol{u}})$ is built from the flux contributions through the control faces, *i.e.*, $\boldsymbol{C}_1$ depends on the fluxes $\bar{u}$ and $\bar{v}$ at the faces of $\Omega_{i,j}$.

The diagonal elements of the coefficient matrix $\boldsymbol{C}_1(\bar{\boldsymbol{u}})$ are equal to half the left-hand side of expression (19), hence they are equal to zero if and only if the interpolations of the temperatures to the control faces are performed with constant weights. Then, the coefficient matrix is skew-symmetric,

$$\boldsymbol{C}_1(\bar{\boldsymbol{u}}) + \boldsymbol{C}_1^*(\bar{\boldsymbol{u}}) = \boldsymbol{0}, \tag{24}$$

like the underlying differential operator.

Next, we consider diffusion. In the continuous case, diffusion corresponds to the symmetric and positive semi-definite operator

$$-\tfrac{1}{\mathrm{Re\,Pr}} \nabla \cdot \nabla. \tag{25}$$

In our approach, we also want its discrete approximation to be symmetric and positive semi-definite. To achieve this, the divergence operator $\nabla\cdot$ in (25) is discretized in a finite volume

fashion, as in (19)–(20). When the boundary conditions for the heat flux are identical to those for the mass flux, the coefficient matrix of the discrete divergence is again given by $\boldsymbol{M}_1^{\mathrm{u}}$ (actually, the divergence operator reads $\boldsymbol{\Omega}_1^{-1}\boldsymbol{M}_1^{\mathrm{u}}$). When the boundary conditions differ, the coefficient matrix $\boldsymbol{M}_1^{\mathrm{u}}$ needs to be modified to incorporate the boundary conditions for the temperature field. The resulting coefficient matrix will be denoted by $\boldsymbol{M}_1$. To preserve the relation between the divergence and gradient operators, the discrete gradient is represented by the negative of the transpose of the discrete divergence. Then, the discrete analogue of (25) becomes $\boldsymbol{\Omega}_1^{-1}\boldsymbol{D}_1$, where the coefficient matrix $\boldsymbol{D}_1$ is given by

$$\boldsymbol{D}_1 = \tfrac{1}{\mathrm{Re\,Pr}}\boldsymbol{M}_1\boldsymbol{\Omega}_1^{-1}\boldsymbol{M}_1^{*}.$$

The matrix $\boldsymbol{D}_1$ is symmetric, and the quadratic form

$$\boldsymbol{\phi}_h^{*}\boldsymbol{D}_1\boldsymbol{\phi}_h = \tfrac{1}{\mathrm{Re\,Pr}}\left(\boldsymbol{M}_1\boldsymbol{\phi}_h\right)^{*}\boldsymbol{\Omega}_1^{-1}\left(\boldsymbol{M}_1\boldsymbol{\phi}_h\right)$$

is positive for all $\boldsymbol{M_1\phi}_h \neq \boldsymbol{0}$, since the entries of $\boldsymbol{\Omega}_1$ are positive. Hence, the matrix $\boldsymbol{D}_1$ is positive semi-definite, like the underlying differential operator (25).

By compiling the convective and diffusive, symmetry-preserving discretizations, we obtain the following semi-discrete representation of the scalar transport equation

$$\boldsymbol{\Omega}_1\frac{\mathrm{d}\boldsymbol{\phi}_h}{\mathrm{d}t} + \boldsymbol{C}_1(\bar{\boldsymbol{u}})\boldsymbol{\phi}_h + \boldsymbol{D}_1\boldsymbol{\phi}_h = \boldsymbol{0}. \tag{26}$$

The semi-discrete system (26) is stable, meaning that the L2 norm of the scalar ϕ does not increase in time,

$$\frac{\mathrm{d}}{\mathrm{d}t}||\boldsymbol{\phi}_h||_h^2 \overset{(24)}{=} -\boldsymbol{\phi}_h^{*}\left(\boldsymbol{D}_1 + \boldsymbol{D}_1^{*}\right)\boldsymbol{\phi}_h \leq 0,$$

which implies that a solution can be obtained on any grid without adding artificial dissipation.

To turn Equation (26) into a higher-order approximation, we write down the discrete transport energy for the control volume $\Omega_{i,j}^{(3)} = [x_{i-2}, x_{i+1}] \times [y_{j-2}, y_{j+1}]$. Here, it may be noted that we cannot expand the 'original' volumes $\Omega_{i,j}$ by a factor of two (in all directions) since our grid is not collocated. On a staggered grid, three times larger volumes are the smallest possible volumes for which the same discretization rules can be applied as for the 'original' volumes. This yields

$$|\Omega_{i,j}^{(3)}|\frac{\mathrm{d}\phi_{i,j}}{\mathrm{d}t} + \bar{\bar{u}}_{i+1,j}\phi_{i+3/2,j} + \bar{\bar{v}}_{i,j+1}\phi_{i,j+3/2} - \bar{\bar{u}}_{i-2,j}\phi_{i-3/2,j} - \bar{\bar{v}}_{i,j-2}\phi_{i,j-3/2}, \tag{27}$$

where $\bar{\bar{u}}$ and $\bar{\bar{v}}$ denote the mass fluxes through the faces of the larger control volumes $\Omega^{(3)}$. These satisfy the law of conservation of mass:

$$\bar{\bar{u}}_{i+1,j} + \bar{\bar{v}}_{i,j+1} - \bar{\bar{u}}_{i-2,j} - \bar{\bar{v}}_{i,j-2} = 0.$$

As previously, the mass fluxes

$$\bar{\bar{u}}_{i,j} = \int_{y_{j-2}}^{y_{j+1}} u(x_i, y, t)\mathrm{d}y \quad \text{and} \quad \bar{\bar{v}}_{i,j} = \int_{x_{i-2}}^{x_{i+1}} v(x, y_j, t)\mathrm{d}y$$

are discretized by means of the mid-point rule to yield an expression of the form $\boldsymbol{M}_3^{\mathrm{u}}\boldsymbol{u}_h = \boldsymbol{0}$. On a uniform grid, the local truncation errors in $\boldsymbol{M}_1^{\mathrm{u}}\boldsymbol{u}_h = \boldsymbol{0}$ and $\boldsymbol{M}_3^{\mathrm{u}}\boldsymbol{u}_h = \boldsymbol{0}$ are of the order

$2+d$, where $d=2$ in two spatial dimensions and $d=3$ in 3D. The leading term in the discretization error may be removed through a Richardson extrapolation (see also [19]). This leads to the fourth-order approximation of the incompressibility constraint,

$$\boldsymbol{M}_{\mathrm{u}}\boldsymbol{u}_h=\left(3^{2+d}\boldsymbol{M}_1^{\mathrm{u}}-\boldsymbol{M}_3^{\mathrm{u}}\right)\boldsymbol{u}_h=\boldsymbol{0}.$$

The temperatures at the control faces of the large volumes are interpolated in a way similar to that given by (22):

$$\phi_{i+3/2,j}=\tfrac{1}{2}(\phi_{i+3,j}+\phi_{i,j}) \quad \text{and} \quad \phi_{i,j+3/2}=\tfrac{1}{2}(\phi_{i,j+3}+\phi_{i,j}). \tag{28}$$

In matrix-vector notation, we may summarize expressions (27)–(28) as

$$\boldsymbol{\Omega}_3\frac{\mathrm{d}\boldsymbol{\phi}_h}{\mathrm{d}t}+\boldsymbol{C}_3(\bar{\bar{\boldsymbol{u}}})\boldsymbol{\phi}_h, \tag{29}$$

where the diagonal matrix $\boldsymbol{\Omega}_3$ encapsulates the sizes of the large control volumes, and $\boldsymbol{C}_3$ consists of flux contributions ($\bar{\bar{u}}$ and $\bar{\bar{v}}$) through the faces of these volumes.

Again, the leading term in the discretization error may be removed through a Richardson extrapolation yielding

$$\underbrace{\left(3^{2+d}\boldsymbol{\Omega}_1-\boldsymbol{\Omega}_3\right)}_{\boldsymbol{\Omega}}\frac{\mathrm{d}\boldsymbol{\phi}_h}{\mathrm{d}t}+\underbrace{\left(3^{2+d}\boldsymbol{C}_1(\bar{\boldsymbol{u}})-\boldsymbol{C}_3(\bar{\bar{\boldsymbol{u}}})\right)}_{\boldsymbol{C}(\boldsymbol{u}_h)}\boldsymbol{u}_h.$$

The coefficient matrix $\boldsymbol{C}$ of the convective operator depends formally on both $\bar{\boldsymbol{u}}$ and $\bar{\bar{\boldsymbol{u}}}$, since it is constructed from $\boldsymbol{C}_1$ and $\boldsymbol{C}_3$. Yet, since we have applied the mid-point rule to approximate the mass fluxes $\bar{\boldsymbol{u}}$ and $\bar{\bar{\boldsymbol{u}}}$, we may view $\boldsymbol{C}$ as a function of the discrete velocity vector $\boldsymbol{u}_h$ (and thus close the discrete system). Note that the weights 3^{2+d} and -1 are to be used on nonuniform grids too, since otherwise the coefficient matrix $\boldsymbol{C}$ of the discrete, convective operator is not skew-symmetric.

The diffusive term of the scalar transport equation undergoes a similar treatment. This leads to a fourth-order, symmetric, positive semi-definite coefficient matrix

$$\boldsymbol{D}=\tfrac{1}{\mathrm{Re}\,\mathrm{Pr}}\boldsymbol{M}\boldsymbol{\Omega}^{-1}\boldsymbol{M}^{*}.$$

Taking all terms together, the symmetry-preserving, fourth-order discretization of the scalar transport equation (2) becomes

$$\boldsymbol{\Omega}\frac{\mathrm{d}\boldsymbol{\phi}_h}{\mathrm{d}t}+\boldsymbol{C}(\boldsymbol{u}_h)\boldsymbol{\phi}_h+\boldsymbol{D}\boldsymbol{\phi}_h=\boldsymbol{0}. \tag{30}$$

Also the fourth-order, symmetry-preserving discretization (30) is unconditionally stable,

$$\frac{\mathrm{d}}{\mathrm{d}t}||\boldsymbol{\phi}_h||_h^2=\frac{\mathrm{d}}{\mathrm{d}t}\left(\boldsymbol{\phi}_h\boldsymbol{\Omega}\boldsymbol{\phi}_h\right)=-\boldsymbol{\phi}_h^{*}\left(\boldsymbol{D}+\boldsymbol{D}^{*}\right)\boldsymbol{\phi}_h\leq 0,$$

where we have made use of the the skew symmetry of $\boldsymbol{C}(\boldsymbol{u}_h)$ and the nonnegative-definiteness of $\boldsymbol{D}$.

Finally, if we ignore any contribution resulting from boundary conditions, we see that Equation (2) leads to $\frac{\mathrm{d}}{\mathrm{d}t}\int_\Omega\phi\mathrm{d}\Omega=0$. The semi-discrete system (30) maintains the quantity $\boldsymbol{1}^{*}\boldsymbol{\Omega}\boldsymbol{\phi}_h$:

$$\frac{\mathrm{d}}{\mathrm{d}t}\left(\boldsymbol{1}^{*}\boldsymbol{\Omega}\boldsymbol{\phi}_h\right)\overset{(30)}{=}-\left(\boldsymbol{C}^{*}(\boldsymbol{u}_h)+\boldsymbol{D}^{*}\right)\boldsymbol{1}^{*}\boldsymbol{\phi}_h=\boldsymbol{C}(\boldsymbol{u}_h)\boldsymbol{1}^{*}\boldsymbol{\phi}_h-\boldsymbol{D}\boldsymbol{1}^{*}\boldsymbol{\phi}_h=\boldsymbol{0},$$

where both the row sums of $\boldsymbol{C}(\boldsymbol{u}_h)$ and $\boldsymbol{D}$ are zero, as they represent a consistent discretization of a convective and diffusive operator, respectively.

4.2. Time-integration

The equations governing turbulent flow and heat transfer in the channel with surface-mounted cubes are integrated in time by means of an explicit, second-order, one-leg method that is tuned to get the largest possible interval of convective stability. Details about the one-leg method are given in [20]. The one-leg method is applied to both the Navier–Stokes equations (1) and the scalar transport equation (2). Equation (3) does not contain a convective term. Therefore, it is not discretized in time by means of the one-leg method. Instead, we have applied Euler's explicit method.

As the thermal diffusivity of air is approximately two orders of magnitude larger than that of the epoxy, the diffusive time scales in the air flow around a cube and in the epoxy cover of a heated cube differ significantly. Air reacts much faster to temperature changes than epoxy, and it takes much longer to reach an equilibrium state in the epoxy layer than in the air. To shorten the time needed to reach equilibrium, the diffusivity in the epoxy layer of the cube is increased in the beginning, starting from a value that is slightly lower than the diffusivity of air, and then gradually decreased until it reaches its given value.

The thermal coupling between the air and the epoxy layer has been implemented with the help of an overlap. That is, we have defined a ghost air temperature at the centre of the first grid cell inside the heated cube as well as a ghost epoxy temperature at the centre of the first grid cell (in the flow) outside the cube. At the boundary, two conditions are to be satisfied: the air and epoxy temperature are equal, and the heat flux is given by Equation (4). Both are discretized explicitly in time. Their spatial discretization uses the ghost temperatures. From the two discretized boundary conditions, we can solve the ghost epoxy temperature in terms of non-ghost temperatures near the boundary. The resulting expression is stable, and thus the temperature in the epoxy layer can be updated in time. After that, the air temperature is updated, where the ghost air temperature is computed from the Dirichlet condition at the boundary. Thus, the air and cube exchange temperatures and fluxes at their common boundary in an explicit, stable manner.

4.3. Validation numerical method

In this section, we present results of two flows with passive scalar transport to validate the numerical method described in the preceding section.

4.3.1. *Taylor–Green vortex with passive scalar transport*

The symmetry-preserving discretization method was used to carry out numerical simulations of a Taylor–Green vortex flow with passive scalar transport. This is one of the simplest systems where one can study the error by comparing the numerical results with the analytical solution,

$$u = -\cos(x)\sin(y)\ \mathrm{e}^{-\frac{2}{\mathrm{Re}}t}, \qquad v = \cos(y)\sin(x)\ \mathrm{e}^{-\frac{2}{\mathrm{Re}}t}, \qquad w = 0,$$

$$\phi = -\cos(y)\cos(x)\ \mathrm{e}^{-\frac{2}{\mathrm{Re}\,\mathrm{Pr}}t}.$$

The flow domain is 2π-periodic and the initial conditions correspond to $t = 0$. The Reynolds number is taken equal to $\mathrm{Re} = 10$; the Prandtl number is $\mathrm{Pr} = 0{\cdot}71$. Four discretization methods have been investigated: (2L) the second-order method based on Lagrangian interpolation (minimizing local truncation error); (2S) the second-order symmetry-preserving method; (4L) the fourth-order Lagrangian method; (4S) the fourth-order symmetry-preserving method. The

grids are taken piecewise uniform in x and y (and uniform in z). The x- and y-directions are treated equal; we describe the x-mesh. Since the convective derivatives $u\partial_x\phi$ and $v\partial_x\phi$ are proportional to $\sin(2x)$, we want to have a smaller spacing near the zeros of $\sin(2x)$. Thus, the uniform mesh width in the interval $[-\pi/8, \pi/8]$ is half the mesh width in $[\pi/8, 3\pi/8]$ and this piecewise-uniform grid is continued modulo $\pi/2$. Note that the symmetry-preserving discretizations 2S and 4S differ from the Lagrangian methods 2L and 4L only near the interface points where the grid abruptly changes.

To give an impression of the behaviour of the four discretization methods 2L, 4L, 2S and 4S, we present in Figure 4 the global discretization error defined by $||\boldsymbol{\phi}_h - \boldsymbol{\phi}_{\text{exact}}||$ (the norm is the L2 norm and the vector $\boldsymbol{\phi}_{\text{exact}}$ is formed by restricting the analytical solution ϕ to the grid points) as a function of the mean mesh size $2\pi/N$, where N is the number of grid points. It is observed that symmetry-preserving methods show a regular monotone behaviour upon grid refinement. In contrast, the fourth-order Lagrangian method 4L is not even as accurate as its second-order counterpart 2L for coarse grids. This explains why high-order Lagrangian discretization has not been popular. Further, when the number of grid points is low, Lagrangian discretization is much less accurate than symmetry-preserving discretization.

4.3.2. *Channel flow with heat transfer*

Next, the symmetry-preserving simulation method is tested for a turbulent flow with heat transfer in a channel with flat walls. The Reynolds number is set to $\text{Re} = 5{,}600$ (based on the channel width and the bulk velocity) and the Prandtl number is $\text{Pr} = 0{\cdot}71$. At these Reynolds and Prandtl numbers direct numerical simulations have been performed by several research groups; see *e.g.* [21]–[24]. In addition, we can compare the numerical results to experimental data, for instance, to the temperature profiles compiled by Kader [25].

As usual, the flow is assumed to be periodic in the stream- and spanwise directions. Consequently, the computational domain may be confined to a channel unit of dimension $2\pi \times 1 \times \pi$, where the width of the channel is normalized. All computations presented in this section were performed with 64 (uniformly distributed) streamwise grid points, 32 (uniformly distributed) spanwise points and 64 grid points in the direction normal to the wall. The normal grid points are computed according to

$$y_j = \frac{\sinh(j\gamma/64)}{2\sinh(\gamma/2)} \qquad \text{for} \quad j = 0, 1, \ldots, 32,$$

where the stretching parameter γ is equal to 6·5. The grid points in the remaining half of the channel ($1/2 < y_j \leq 1$) are computed by means of symmetry. The grid point nearest the wall is located at $y_1^+ \approx 1{\cdot}4$. The non-dimensional time step is set equal to $\delta t = 1{\cdot}25 \times 10^{-3}$. Mean values of computational results are obtained by averaging the results over the directions of periodicity, the two symmetrical halves of the channel, and time. The averaging over time starts after a start-up period. The start-up period as well as the time-span over which the results are averaged, 1500 non-dimensional time-units, are identical for all the results.

Here, we consider the temperature profiles only. In [1], we compared the mean and root-mean-square velocity as obtained from our symmetry-preserving simulation to those of other DNSs [21]–[23] and to the experiment by Kreplin and Eckelmann [26]. The agreement with both the numerical and experimental reference data was excellent.

Figure 5 displays a comparison of mean temperature profiles. The agreement between our results and the computational results of Kasagi *et al.* [24] is good. Here, it may be noted that Kasagi *et al.* use 16 times our grid points. The agreement between the numerical results

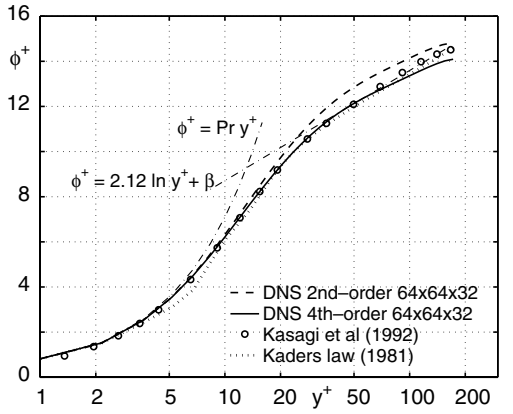

Figure 5. Comparison of the mean temperature ϕ^+ as function of y^+ in a plane channel. The dashed lines represent the law of the wall and the log law. Kader's data provides the best fit through a large number of experiments (performed at a large range of Reynolds numbers). The value of the constant β is taken from [25].

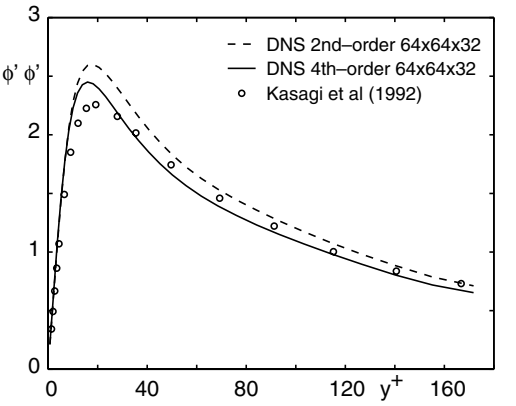

Figure 6. Comparison of $\overline{\phi'\phi'}$ for fully-developed channel flow.

and Kader's formula [25] (which is based on a large number of experimental results in a wide range of Re and Pr) is also good.

Second- and fourth-order results are compared in Figures 5 (mean temperature) and 6 (fluctuating temperature). The results of the second-order discretization method agree less with the reference data than those of the fourth-order method. Therefore, we will use the fourth-order discretization to simulate the flow and heat transfer in the channel with surface mounted cubes.

5. Flow and heat transfer in the channel with the surface-mounted cubes

This section consists of two parts. The first part (Section 5.1) contains the results of the simulation of the flow field; the second part deals with the temperature (Section 5.2). Unless stated otherwise, the sub-channel unit (shown in Figure 1) is covered by a 100^3 staggered grid that is stretched away from both the cubes and the channel walls. The first grid-point away from a cube (or a wall) is located at $0{\cdot}006h$. A cube is represented by 40 grid points in each direction. The grid is continued inside the heated cube.

5.1. Flow

The temporal behavior of the flow is analyzed with the help of a time series of the fluctuating streamwise velocity v' at a station in the wake of the cube. From this time series, the auto-correlation

$$\rho(t) = \overline{v'(t_0)v'(t-t_0)} / \overline{v'(t_0)^2}$$

has been computed and the result is shown in Figure 7. The first positive peak of $\rho(t)$ occurs at $t = 2{\cdot}7$ (that is, after 1800 time steps). This time corresponds to the shedding period. Note that we have non-dimensionalized time by means of the bulk velocity and the channel height. For this type of flow, however, the shedding period is usually measured in terms of the bulk

velocity and the cube height. In that measure, the shedding period becomes 3·4 times larger, and the Strouhal number is

$$St = 0{\cdot}109.$$

This value is exactly (in three digits) equal to Strouhal number obtained from the experimental data; see [15].

The second derivative of the auto-correlation $\rho(t)$ at time $t = 0$ is approximately -200. This gives a Taylor micro-scale of approximately 5×10^{-3} (again non-dimensionalized by means of the bulk velocity and the channel height). This value is in good agreement with that determined from the experiments, which give a Taylor micro-scale of 5×10^{-3} plus/minus ten percent [15].

Figure 7 shows that the auto-correlation function can be seen as a superposition of Fourier-modes. In Fourier space, the auto-correlation decays with a power of $-1{\cdot}55$. This value is somewhat larger than $-5/3$ which is usually found in turbulent spectra (for the inertial subrange). This difference may be caused by the fact that the Reynolds number is not high enough and/or by wall effects. Anyhow, the power-density spectrum calculated from the experimental data decays with a power of approximately $-1{\cdot}6$ (see [15, Figure 8.13]), *i.e.*, also with a power that is (slightly) larger than $-5/3$.

To illustrate the convergence upon grid refinement, we have also performed a simulation on a 60^3 grid. The first grid point of the 60^3 grid lies approximately one and a half times farther from the wall than that of the 100^3 grid. The mean-square of the fluctuating spanwise velocity $\overline{w'w'}$ of fine grid simulation, the coarse grid simulation, and the experiment of Meinders *et al.* are shown in Figure 8. As can be seen, the 100^3 simulation predicts the mean-square of the fluctuating spanwise velocity correctly, while the 60^3 simulation is far off. In particular, it predicts the extremal values of the mean-square of the fluctuating spanwise velocity wrong. The peak of $\overline{w'w'}$ near the cube of the 60^3 simulation is approximately 70%

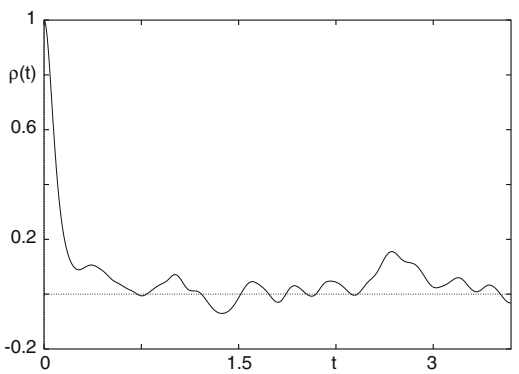

Figure 7. The normalized auto-correlation $\rho(t)$ of a fluctuating streamwise velocity in the wake of the cube as function of time t. The peak at $t = 2{\cdot}7$ corresponds to the shedding period. The negative peak at $t = 1{\cdot}35$ indicates the half of the shedding period.

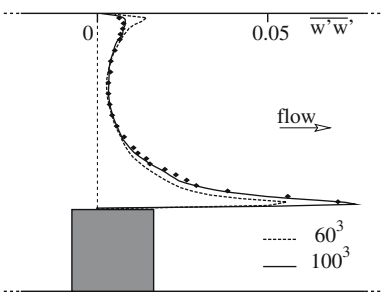

Figure 8. A comparison of the mean-square of the fluctuating spanwise velocity at a cross-section of the channel. The cross-section is taken perpendicular to the spanwise direction and bisects the cube. The geometry is drawn to scale. The continuous line corresponds to the 100^3 simulation; the dashed line denotes the 60^3 simulation; the experimental data are depicted by the dots.

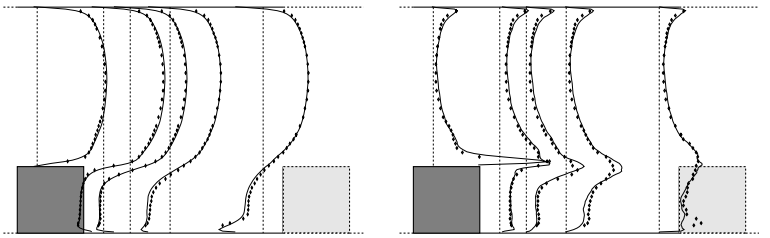

Figure 9. Comparison of first-order statistics (left picture) and second-order statistics (right picture) of the DNS with experimental data. Shown are the mean streamwise velocity $\overline{u}$ (upper picture) and $\overline{u'u'}$ (lower picture) in the plane parallel to the streamwise direction that bisects the cubes. The continuous lines correspond to the DNS; the experimental data are depicted by the dots.

of that of the 100^3 simulation. The peak near the flat wall is about 100% larger than that of the 100^3 simulation.

The statistics of the flow have been averaged over 40 shedding cycles. First- and second-order statistics of the velocity field obtained from the 100^3 simulation at the cross section of the channel that bisects a cube are compared to the avaliable experimental data in Figure 9. The profiles of the mean streamwise velocity and the mean-square of the fluctuating streamwise velocity are in good agreement with the experiments, except in front of a cube where some discrepancies between the mean-squares of the fluctuating streamwise velocities exist. In conclusion, the 100^3 simulation reproduces the turbulent flow field reasonably well.

5.2. Heat transfer

Meinders *et al.* [14], [15] measured the temperature at the surface of the heated cube by means of infrared thermography. At each face, they measured the surface temperature at a grid of 30^2 points. Liquid crystals were used to correct for the spatial image degradation of the infrared camera used.

Average temperatures per face of the heated cube are compared in Table 1. Here, q_{cond} denotes the conductive heat flux through epoxy layer, q_{conv} represents the convective heat flux, and q_{rad} stands for the radiative heat flux. The average temperature per face is denoted by ϕ_{face}. All quantities are given in the same physical dimensions as in the experiment. As can be seen, the average surface temperatures of the simulation are lower than in the experiment. The largest difference occurs at the top face of the cube where the computed average surface temperature is approximately 7% lower than the measured temperature. The average

Table 1. Averaged heat fluxes and temperatures per cube face. A comparison of numerical results with experimental data.

face	experiment				simulation			
	q_{cond} W/m^2	q_{conv} W/m^2	q_{rad} W/m^2	ϕ_{face} °C	q_{cond} W/m^2	q_{conv} W/m^2	q_{rad} W/m^2	ϕ_{face} °C
windward	2976	2762	214·4	51·50	2775	2581	193·6	48·44
top	2592	2364	227·9	53·35	2687	2486	201·3	49·51
leeward	2084	1821	262·6	57·95	1717	1466	251·0	56·18
side I	2676	2445	230·6	53·74	2505	2295	210·1	50·73
side II	2597	2363	234·3	54·23	2505	2295	210·1	50·73

temperatures at two side faces (side I and side II) of the cube should be equal by symmetry. The same applies to the fluxes at the two side faces. The experimental results do not satisfy the symmetry perfectly due to errors in the measurements. The difference between the experimental results at the two side faces gives an idea of the magnitude of the error in the experiment.

The time-averaged temperatures along some paths at the surface of the heated cube are compared to those of the experiment in Figure 10. A number of measuring points lie on the intersection of two paths. At these points, two data points are available. Both are shown in Figure 10 to illustrate the uncertainty in the experimental data. Given this uncertainty, we may conclude that the experimentally and numerically obtained mean temperatures agree. Yet,

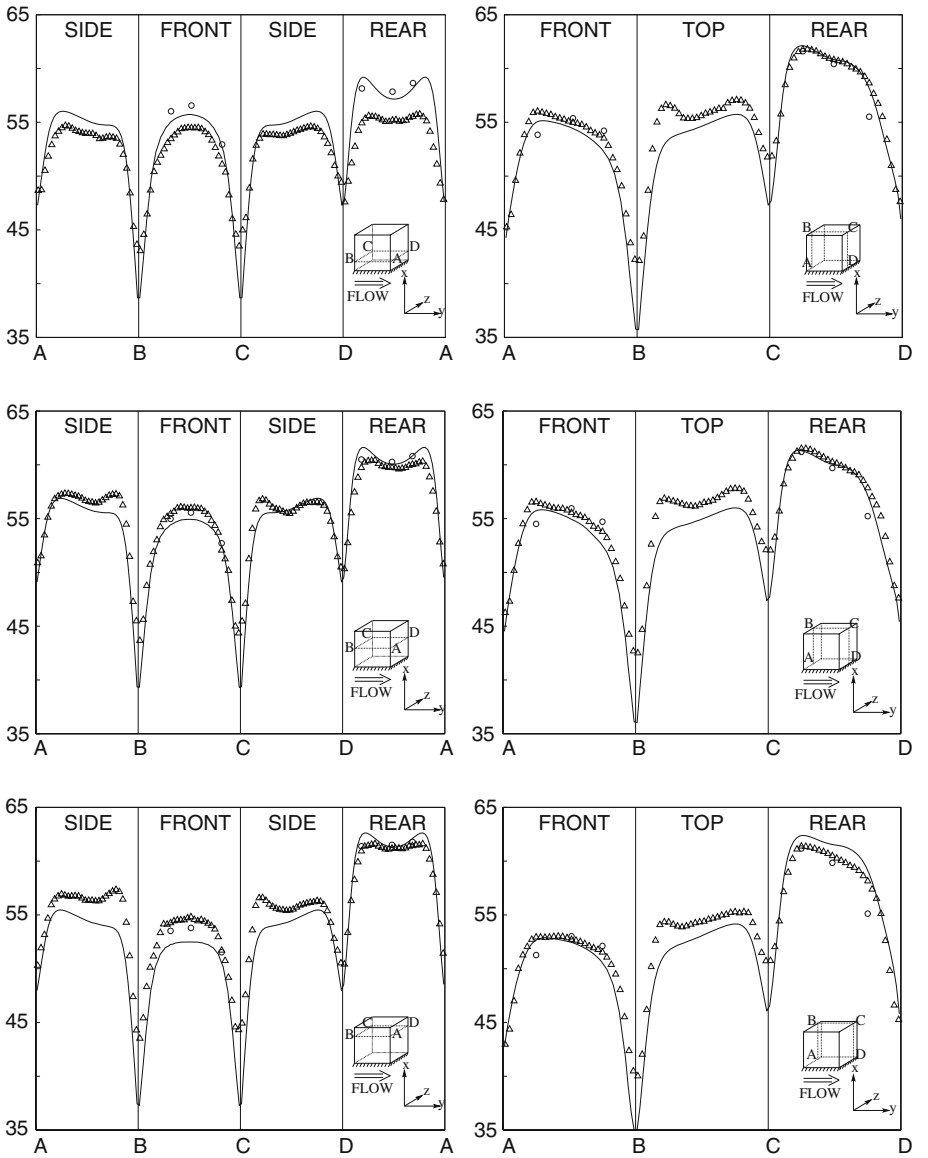

Figure 10. The mean temperature along different paths at the surface of the heated cube. The markers denote the experimental data by Meinders *et al.* [14]. Note that, at three points along BC and DA (left-hand column), and at three points along AB and CD (right-hand column), two data-points are available, depicted by circles and triangles, respectively.

at the edges, the numerical simulation predicts a temperature that is lower than the measured temperature. The difference may become as large as 5° C, which is about 10% deviation.

6. Concluding remarks

Convection transfers energy from the scales at which the flow is driven to the smallest scales that can survive viscous dissipation. The balance between convective transport and viscous dissipation is mathematically described by two differential operators differing in symmetry: the convective derivative is skew-symmetric, whereas diffusive is symmetric and positive-definite. If the Lagrangian discretization scheme is applied (that is, the discretization is constructed to minimize the local truncation error), the skew-symmetry of the convective derivative is lost on nonuniform grids. Therefore, we have developed a spatial discretization method which preserves symmetry. The symmetry-preserving discretization method inherits all conservation and stability properties from the continuous formulation. Second-order and fourth-order versions have been developed for structured, non-uniform grids. In principle, the method can be applied to any convection-diffusion equation. In this paper, it is applied to the Navier–Stokes equations as well as to the passive transport of a scalar.

The results of the symmetry-preserving simulation method can be summarized as follows:

- When the number of grid points is low, the Lagrangian discretization appears to be less accurate than the symmetry-preserving discretization alternative for a Taylor-Green vortex with passive scalar transport.
- For a channel with flat walls, the results of the fourth-order, symmetry-preserving discretization method agree better with the reference data than those of the second-order method.
- The fourth-order, symmetry-preserving discretization method yields good results for the flow and heat transfer in the channel with surface mounted cubical obstacles. The turbulent flow profiles agree well with available experimental data. The same holds for the time-averaged surface temperatures, except for the edges of the cube where differences up to 10% arise.

In summary, the paper presents a new numerical method that enforces important symmetry-preserving properties of the Navier–Stokes equations and performs well in several tests, including comparison with experiments.

References

1. R.W.C.P. Verstappen and A.E.P. Veldman, Symmetry-preserving discretization of turbulent flow. *J. Comp. Phys.* 187 (2003) 343–368.
2. T.A. Manteufel and A.B. White, Jr., The numerical solution of second-order boundary value problems on nonuniform meshes. *Math. Comp.* 47 (1986) 511–535.
3. Y. Morinishi, T.S. Lund, O.V. Vasilyev and P. Moin, Fully conservative higher order finite difference schemes for incompressible flow. *J. Comp. Phys.* 143 (1998) 90–124.
4. O.V. Vasilyev, High order finite difference schemes on non-uniform meshes with good conservation properties. *J. Comp. Phys.* 157 (2000) 746–761.
5. F. Nicoud, Conservative high-order finite-difference schemes for low-Mach number flows. *J. Comp. Phys.* 158 (2000) 71–97.
6. F. Ducros, F. Laporte, T. Soulères, V. Guinot, P. Moinat and B. Caruelle, High-order fluxes for conservative skew-symmetric-like schemes in structured meshes: application to compressible flows. *J. Comp. Phys.* 161 (2000) 114–139.
7. A. Jameson, W. Schmidt and E. Turkel, Numerical solutions of the Euler equations by finite volume methods using Runge-Kutta time stepping. AIAA Paper 81-1259 (1981) 19pp.

8. D. Furihata, Finite difference schemes for $\frac{\partial u}{\partial t} = \left(\frac{\partial}{\partial x}\right)^{\alpha} \frac{\delta G}{\delta u}$ that inherit energy conservation or dissipation property. *J. Comp. Phys.* 156 (1999) 181–205.
9. J.M. Hyman, R.J. Knapp and J.C. Scovel, High order finite volume approximations of differential operators on nonuniform grids. *Physica D* 60 (1992) 112–138.
10. K. Hanjalić and S. Obi (eds.), *Proceedings of the 6th ERCOFTAC/IAHR/COST Workshop on Refined Flow Modeling*. Delft: Delft University of Technology (1997) 129pp.
11. T. Craft (ed.), *Proceedings of the 7th ERCOFTAC/IAHR/COST Workshop on Refined Flow Modeling*. Manchester: University of Manchester Institute of Science and Technology (1998) 87pp.
12. A. Hellsten and P. Rautaheimo (eds.), *Proceedings of the 8th ERCOFTAC/IAHR/COST Workshop on Refined Flow Modeling*. Helsinki: Helsinki University of Technology (1999) 96pp.
13. F. Mathey, J. Fröhlich and W. Rodi, Large-eddy simulation of the flow over a matrix of surface-mounted cubes. In: S. Biringen *et al.* (eds.), *Industrial and Environmental Applications of Direct and Large-Eddy Simulation* Springer Lecture Notes in Physics. Vol. 529. Berlin: Springer-Verlag (1999) pp. 153–163.
14. E.R. Meinders, Th.H. van der Meer, K. Hanjalić and C.J.M. Lasance, Application of infrared thermography to the evaluation of local convective heat transfer on arrays of cubical protrusions. *International J. Heat and Fluid Flow* 18 (1997) 152–159.
15. E.R. Meinders, *Experimental Study of Heat Transfer in Turbulent Flows over Wall-Mounted Cubes*. Ph.D. thesis, Delft: Delft University of Technology (1998) 146pp.
16. C. Foias, O. Manley, R. Rosa and R. Temam, *Navier-Stokes Equations and Turbulence*. Cambridge: Cambridge University Press (2001) 347pp.
17. F. Zhang, *Matrix Theory*. New-York: Springer-Verlag (1999) 277pp.
18. F.H. Harlow and J.E. Welsh, Numerical calculation of time-dependent viscous incompressible flow of fluid with free surface. *Phys. of Fluids* 8 (1965) 2182–2189.
19. M. Antonopoulos-Domis, Large-eddy simulation of a passive scalar in isotropic turbulence. *J. Fluid Mech.* 104 (1981) 55–79.
20. R.W.C.P. Verstappen and A.E.P. Veldman, Direct numerical simulation of turbulence at lower costs. *J. Engng. Math.* 32 (1997) 143–159.
21. J. Kim, P. Moin and R. Moser, Turbulence statistics in fully developed channel flow at low Reynolds number. *J. Fluid Mech.* 177 (1987) 133–166.
22. N. Gilbert and L. Kleiser, Turbulence model testing with the aid of direct numerical simulation results. In: *Proceedings Turbulent Shear Flows 8*, Paper 26-1, Munich: Technical University Munich (1991) pp. 26-1-1 – 26-1-6.
23. A. Kuroda, N. Kasagi and M. Hirata, Direct numerical simulation of turbulent plane Couette-Poisseuille flows: effect of mean shear rate on the near-wall turbulence structures. In: F. Durst *et al., Proceedings Turbulent Shear Flows 9*, Berlin: Springer-Verlag (1995) pp. 241–257.
24. N. Kasagi, Y. Tomita and A. Kuroda, Direct numerical simulation of passive scalar field in a turbulent channel flow. *ASME J. Heat Transfer* 114 (1992) 598–606.
25. B.A. Kader, Temperature and concentration profiles in fully turbulent boundary layers. *International J. Heat and Mass Transfer* 24 (1981) 1541–1544.
26. H.P. Kreplin and H. Eckelmann, Behavior of the three fluctuating velocity components in the wall region of a turbulent channel flow. *Phys. Fluids* 22 (1979) 1233–1239.